Photophysical Studies of Helicate and Mesocate Double-Stranded Dinuclear Ru(II) Complexes

Xinyue Xu,[†,¶] Samuel J. P. Marlton,[†] Kate L. Flint,[‡] Rohan J. Hudson,[†,¶] F. Richard Keene,[‡] Christopher R. Hall,[*,†,¶] and Trevor A. Smith[*,†,¶]

†*School of Chemistry, The University of Melbourne*

‡*Discipline of Chemistry, School of Physics, Chemistry and Earth Sciences, University of Adelaide*

¶*ARC Centre of Excellence in Exciton Science*

E-mail: christopher.hall@unimelb.edu.au; trevoras@unimelb.edu.au

Abstract

The metal-ligand charge transfer (^{3}MLCT) and the phosphorescence-quenching metal-centered (^{3}MC) states of the helicate and mesocate conformers of a double-stranded dinuclear polypyridylruthenium(II) complex have been investigated using ultrafast transient absorption spectroscopy. At 294 K, transient signals of the helicate decayed significantly slower than the mesocate, whereas at 77 K, no clear contrast in kinetics was observed. Contributions to excited-state decay from high-lying ^{3}MLCT states were identified at both temperatures. Spectroscopic data (294 K) suggest that the ^{3}MC state of the helicate lies above the ^{3}MLCT and the reverse is true for the mesocate; this was further validated by DFT calculations. The stabilization of the ^{3}MC state relative to the ^{3}MLCT state in the mesocate was explained by a reduction in ligand field strength due to distortion near the ligand bridge which causes further deviation from octahedral geometry compared to the helicate. This work illustrates how minor structural differences can significantly influence excited state dynamics.

TOC Graphic

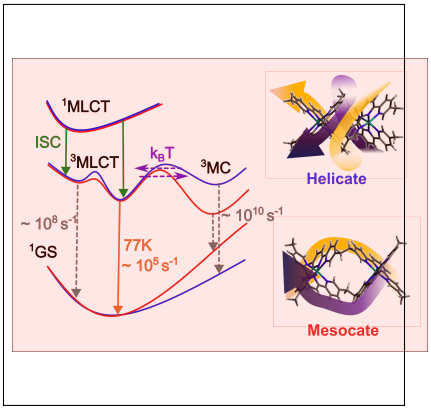

Keywords

photophysics, double-stranded, dinuclear, Ruthenium complexes

Introduction

Transition metal complexes have been widely studied for applications in photochemistry, materials sciences, electronics, and related fields.[1–4] This is partially due to their structure, which can be precisely controlled to tune excitation transition energies and optimize solubility while maintaining chemical inertness in the excited state.[5–7] The long-lived excited states and red emission of polypyridylruthenium(II) complexes afford advantages in applications such as biological imaging, and their photophysical properties have therefore been widely studied.[8–10] Excitation of the absorption band centered at 450 nm excites the ^{1}MLCT state, which is followed by fast intersystem crossing (ISC, $\tau \sim 100$ fs) to the red-emitting ^{3}MLCT state ($\lambda_{max} \sim 600$ nm).[11–13] This lowest ^{3}MLCT is actually a manifold of closely-spaced states that have small energy splittings. These closely-spaced states overlap and are therefore inseparable at non-cryogenic temperatures.[14,15] However, not all polypyridylruthenium(II) complexes have desirable red-emission at ambient temperatures; most bis(tridentate)ruthenium(II) e.g. $[Ru(II)(tpy)_2]^{2+}$ (tpy = 2;2';6',2"-terpyridine) complexes have very low emission quantum yield at room temperature. Kinetic investigations on such complexes[16,17] suggest luminescence quenching occurs when the ^{3}MLCT approaches resonance with a ^{3}MC state ($^5t_{2g}{}^1e_g$, this state is also noted interchangeably as the *dd* state).[18,19] Other studies have proposed an additional pathway: deactivation through a higher ^{3}MLCT state with greater singlet character that lies ca. 500 cm^{-1} above the lowest ^{3}MLCT state.[12,20]

Ultrafast photophysical studies of multinuclear ruthenium compounds have received less attention compared to their mononuclear counterparts, however, these systems are seeing renewed interest as advances in ligand engineering have afforded dinuclear complexes with specific DNA selectivity, and pH sensitivity.[21–24] In cases where the two ruthenium atoms are linked by a conjugated bridge, these complexes may exhibit electronic coupling between the two centers, acting like molecular "wires", with applications that may include light-harvesting materials.[25,26 27,28] Another variation involves a multidentate template ligand that binds to both metal centers at the same time. If two or more such ligands are used to bind to

two metal centers, the complex may be formed in two diastereoisomers: the helicate and the mesocate.[29] The former structure resembles the natural helix shape of DNA and the latter structure has the two ligands on opposite faces of the metal ions. Photophysical properties of helicate and mesocate dinuclear metal complexes are rarely reported, with one example published by Shankar et al., showing structure-dependent luminescent properties.[30]

In 2019, Flint et al. reported the synthesis of double-stranded di-ruthenium(II) complexes in both the helicate and the mesocate diastereoisomers, based on the ligand 1,2-bis{5-(5″-methyl-2,2′:6′,2″-terpyridinyl)}ethane.[31]These compounds have potential applications for targeted cancer therapy as selective binding and cytotoxicity in colorectal cancer cells have been demonstrated in similar ruthenium-containing linear helicates and mesocates.[32] In this report, we investigate the effect of ligand-binding geometry on the photophysical properties of these double-stranded dinuclear Ru(II) complexes with temperature-dependent transient absorption spectroscopy (TAS), and employ computational chemistry to explore the molecular origin of the key observations. Whilst at 77 K, the two isomers do not show a clear contrast in the kinetics, at room temperature, the excited state of the mesocate decayed much faster than the helicate. Equilibrium constants extracted from the global targeted analysis and triplet state energies calculated using DFT showed that ^{3}MC lies below the ^{3}MLCT for the mesocate, leading to faster deactivation of the ^{3}MLCT. The reverse is found for the helicate.

Results and discussion

Steady-state spectroscopy

The absorption (at room temperature) and emission spectra at 77 K of the two complexes in *n*-butyronitrile (Fig. 1) are structurally similar. In the visible region, the absorption bands are broad and lie between 400 nm and 600 nm peaking at 475 nm ($\varepsilon > 10000$ cm^{-1}M^{-1}). These are assigned to vibronic states of the lowest ^{1}MLCT $\leftarrow$ GS transition.[2,33] Excitation

spectra (SI Section 1) extracted from the excitation-emission matrices showed that this broad peak consists of three bands centered at 442 nm, 475 nm, and 515 nm, respectively, which are attributed to the vibrational energy levels of the lowest singlet (vibronic energy level spacing $\sim$1600 cm^{-1}). Based on TD-DFT simulated spectra and calculated molecular orbitals (SI Section 2.5), the visible-region absorption band consists of multiple transitions from metal-based d orbitals of different symmetries to π^* orbitals located on the ligands. The nature of these transitions is discussed in further detail in the following section. The emission at 77 K shows a vibronic progression of three peaks for the ^{3}MLCT $\rightarrow$ GS transition with central wavelengths 602 nm, 643 nm, and 702 nm.

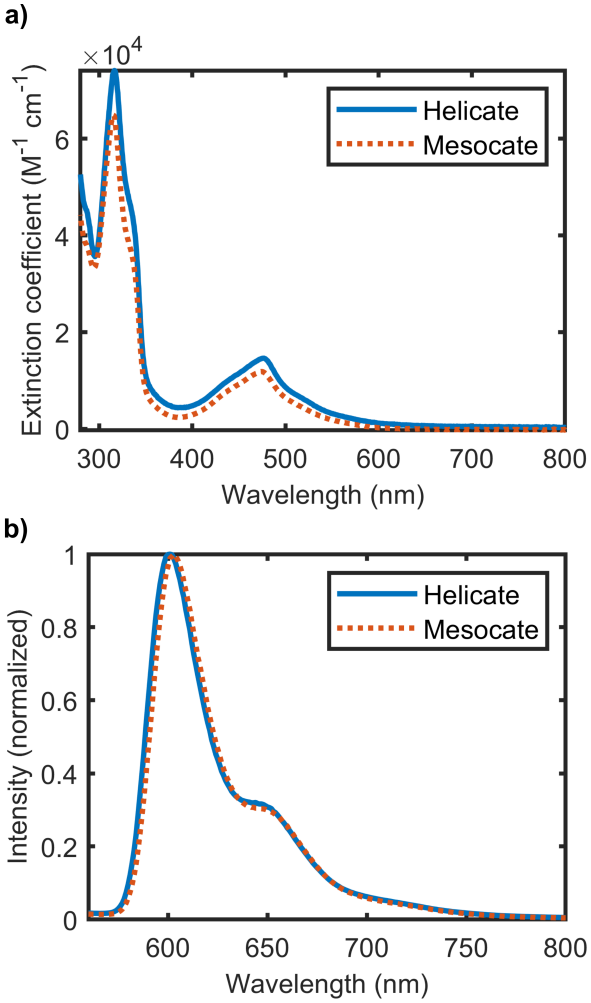

Figure 1: a) Steady-state absorption spectra of helicate and mesocate forms of the dinuclear [Ru(II)(tpy)$_2$]$^{2+}$ derivatives in n-butyronitrile. b) Normalized emission spectra at 77 K in n-butyronitrile glass (λ_{ex} = 477 nm).

Transient Absorption Spectroscopy (TAS)

TAS spectra of the helicate and the mesocate at 294 K and 77 K are shown in Fig. 2 a) and e) and Fig. 3 a) and d). The negative ground state bleach (GSB) is observed below 540 nm, while a broad excited-state absorption (ESA) spanning the red to the near IR (NIR) region is assigned to a ligand-metal charge transfer (LMCT) transition.[19,34–36] Previous studies employing transient absorption[37] and spectro-electrochemistry[38] on conjugated bridge systems showed similar absorption maxima in the NIR region, arising from either excited state delocalization or intervalence charge transfer; both processes involve the one-electron reduced π^* orbital on the ligand. The transient signal of the mesocate decays much faster compared to the helicate. In both cases, the spectral features change with time. The shoulder-like feature from 550 nm to 590 nm and the ESA peak at 800 nm becomes less pronounced at longer delay times and cannot be described by a single component.

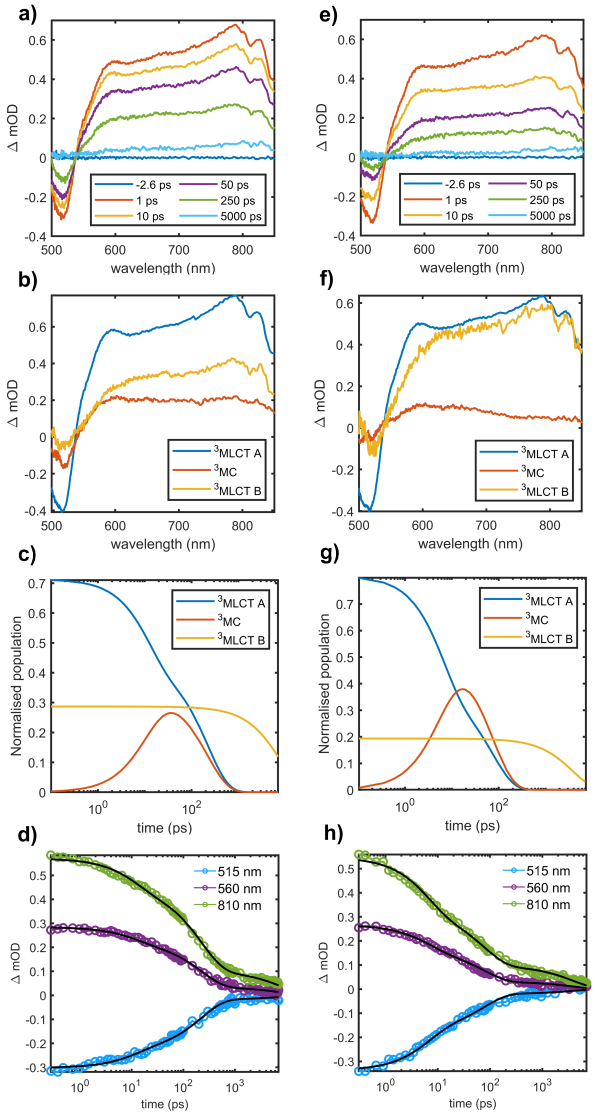

Figure 2: Room temperature TA data of the helicate a) - d) and the mesocate e) - h) in deaerated acetonitrile (λ_{ex} = 440 nm). For c) and g) the normalized population refers to the fractional contribution of the SADS to the overall kinetics

Previous work[16,18] has shown that a pre-equilibrium step exists between the ^{3}MLCT and the ^{3}MC states, with the close-lying ^{3}MLCT states behaving as a single entity at room temperature. Those data were fit with a three-state model, $^3\text{MLCT} \underset{k_2}{\overset{k_1}{\rightleftharpoons}} {}^3\text{MC} \xrightarrow{k_3} \text{GS}$. Our experimental data were globally fitted with this kinetic scheme, however, this model did not provide a good fit (SI Section 3.6 and Fig. S17). The data were better described with an additional independent decay channel with spectral characteristics of the ^{3}MLCT state, here labelled ^{3}MLCT B (Scheme 1).

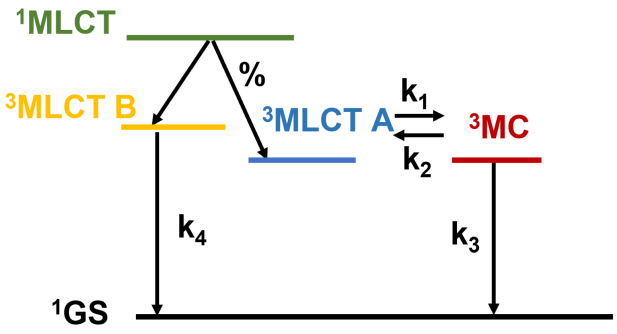

Scheme 1: The kinetic scheme used to fit room temperature TAS data (energy levels are placed qualitatively; the % assigns a fractional splitting to ^{3}MLCT A after intersystem crossing and the remaining decay is via ^{3}MLCT B.

Additional terms that couple this state to either ^{3}MLCT A or ^{3}MC led to unreliable fitting results, so were not included. In many polypyridylruthenium(II) complexes, a higher ^{3}MLCT state has been shown to contribute to non-radiative decay based on results of fitting data using temperature-dependent single-exponential decay components with rates described by Arrhenius-type equations.[39,40] The inclusion of ^{3}MLCT B is used to account for this deactivation pathway via the higher ^{3}MLCT state. The timescale of the ISC process is within the time-resolution of the measurement, so the initial excited-state population is considered to immediately populate either ^{3}MLCT state A or state B. The initial fractional population was included as a constrained parameter (see SI Section 3.2 for fitting details). Fig. 2 b) and f) show the species-associated decay spectra (SADS) from the targeted global fitting of the helicate and the mesocate, respectively, with fitted decay traces at selected wavelengths in the bleach and ESA region presented in d) and h). The best-fit rate parameters from this model are presented in Table 1.

Table 1: Rate parameters of transient absorption fitting (room temperature)

	k_1 (10^{10} s^{-1})	k_2 (10^{10} s^{-1})	k_3 (10^{10} s^{-1})	k_4 (10^{8} s^{-1})	% in MLCT A [b]	K_{eq}
Helicate	3.73 (0.01)[a]	4.24 (0.01)	1.02 (0.01)	1.25 (0.08)	71 (0.1)	0.88
Mesocate	9.36 (0.01)	5.61 (0.01)	2.23 (0.01)	2.63 (0.14)	80 (0.1)	1.67

[a] 2σ confidence bounds are given by covariance matrix where applicable.
[b] % is determined by the relative contribution of the SADS to the overall kinetics

The kinetic analysis and DFT results both suggest that the ^{3}MLCT and ^{3}MC states are

energetically close together. The equilibrium constant for ^{3}MLCT A $\underset{k_2}{\overset{k_1}{\rightleftharpoons}}$ ^{3}MC ($K_{eq} = k_1/k_2$) is 0.88 for the helicate and 1.67 for the mesocate, and the population of the ^{3}MC state is either lower or of similar magnitude compared to the population of the ^{3}MLCT at all delay times (Fig. 2 c) and g)). Therefore, the SADS in blue likely represents the equilibrium mixture with the population mostly in the ^{3}MLCT state, and that in red represents the population in the ^{3}MC state.

In the region below 600 nm in the SADS, the ESA overlaps the GSB features, and due to the bandwidth limit of the probe and excitation scatter, the assignments of the nature of states is difficult based on GSB features. The rationale for assigning the SADS with more ^{3}MC character is as follows. Excitation delocalization or charge transfer involving π^* orbitals on the ligand is sometimes evident by a characteristic feature at 800 nm, which is absent here.[37] The broad ESA spanning this spectral region with low intensity is tentatively assigned to spin-allowed transitions of the ^{3}MC state, and the lowered transition strengths is consistent with the elongated Ru-N bonds in the ^{3}MC state.[19] Negligible ligand dissociation was observed when comparing steady-state absorption spectra before and after prolonged photo-illumination, suggesting the SADS does not represent a photo-decomposition product (SI Section 3.4). Additionally, the rate of relaxation to the ground state (k_3) falls in the range reported for ^{3}MC states for a variety of Ru polypyridyl complexes.[41]

The third component (yellow in Fig. 2 and Fig. 3) extracted has a maximum at $\sim$ 800 nm and red-weighted ESA, which decays with a rate constant of $\sim 10^8$ s^{-1}. The presence of this absorption maximum (characteristic of the one-electron reduced ligand) suggests that it is most likely a ^{3}MLCT state rather than a ^{3}MC state. It should be noted that while the targeted kinetic model used here only fits a percentage contribution and a ground-state relaxation pathway for the ^{3}MLCT B state, inter-conversion between this state and the lower ^{3}MLCT A state could occur at room temperature. The decay rate of the parallel channel (^{3}MLCT B) is most likely limited by the barrier-crossing process from the lower ^{3}MLCT state which is within the range $10^7 \sim 10^8$ s^{-1} reported for a series of $[Ru(tpy)_2]^{2+}$

derivatives, which is slow compared to the timescale of the observed dynamics.[12,39,40,42]

Additionally, the calculated potential energy curve from the ^{3}MLCT state to the ^{3}MC state (details of calculation/interpolation methods are provided in SI Section 2.4) presented in Fig. 4 shows a smaller upper bound of the crossing barrier (ΔE_{TS} in Fig. 2) for the mesocate compared to the helicate, as well as a smaller gap to the ground state energy curve. The faster rate parameters k_1 (Arrhenius-type behavior) and k_3 (energy gap law) are qualitatively consistent with the computational result. The difference between the triplet manifolds of the helicate and the mesocate is subtle but perceptible. $K_{eq} < 1$ places the ^{3}MC state above the ^{3}MLCT state for the helicate and the reverse for the mesocate, again, consistent with computational results. Previous studies have suggested that torsional strain posed by ligands that distorts the complex from a perfectly octahedral coordination environment will weaken the ligand field strengths and stabilize the ^{3}MC state.[16] Indeed, by examining the crystal and DFT-optimized ground-state structures, the mesocate is more distorted as the N-Ru-N angle from the one axial nitrogen to the nitrogen nearest the ethylene bridge on the opposite ligand is 99° for the helicate, but is 105° for the mesocate. An unstrained octahedral environment will have an angle close to 90° and for the monomeric $Ru[(tpy)]_2]^{2+}$ structure optimized with the same level of theory, this angle is 100°. Additionally, in the DFT optimized ground state geometry, the Ru-N bond length to the nitrogen closest to the bridge is ~ 0.015 Å longer in the mesocate compared to the helicate; this also indicates that the mesocate structure causes the coordination environment to further deviate from octahedral (calculated and crystallography bond lengths and angles can be found in SI Section 2.1).

We also performed TAS at 77 K to further investigate the ^{3}MLCT states that are thermally populated and overlapping at room temperature (Fig. 3). Note that the timescale of these low temperature measurements is longer than at room temperature (Fig. 2). Identification of states is aided by restricted population transfer to the ^{3}MC state at low temperature, isolating the ^{3}MLCT manifold.[43,44] For $[Ru(tpy)_2]^{2+}$, a complex related to the monomeric

unit of the two conformers, only one ^{3}MLCT structure was observed by a previous computational study.[45] However, it is well accepted in the literature that the lowest ^{3}MLCT state is split into many near-degenerate states by SOC.[14,15,39]

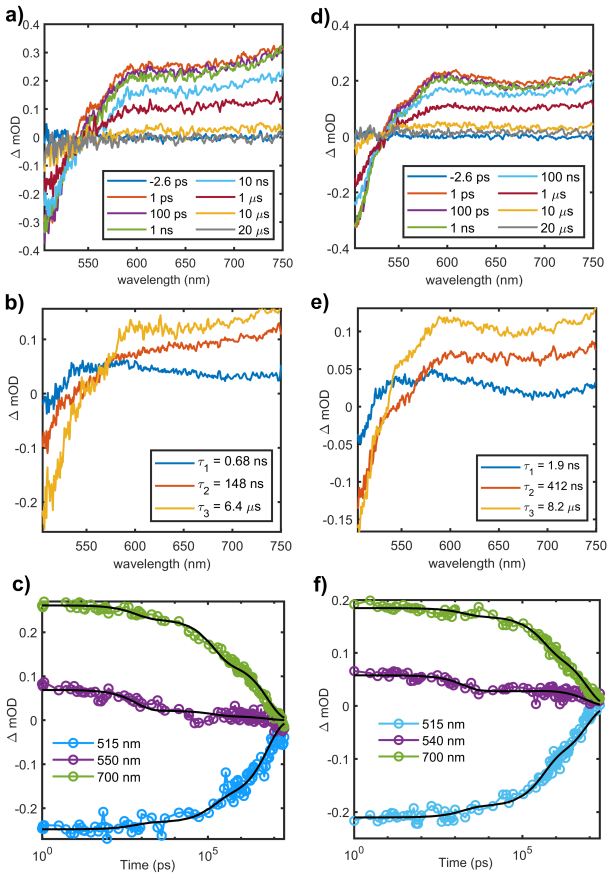

Figure 3: Cryogenic TA data of the helicate a) - c) and the mesocate d) - f) in glassy *n*-butyronitrile at 77K (λ_{ex} = 477 nm). Note that lowered transmission of probe intensity in the NIR region does not give sufficient signal-to-noise ratio to resolve kinetics in this region, so the data are only presented up to 750 nm

.

The TA difference spectra at 77 K are slightly different from the room temperature equivalents. From 1 ps to several ns, there is little change in the GSB intensity, while the the ESA in the 600 nm to 700 nm region decreases in intensity. Both complexes have faster decay rates ($\sim 5 \times 10^5$ s^{-1}) than typically reported for $[Ru(II)(tpy)_2]^{2+}$ at 77 K.[12,46] The transient kinetics are not well-described by mono- or bi-exponential models. This points to the possibility that multiple almost isoenergetic states are accessed in the triplet manifold

even without much thermal energy (kT = 53.5 cm^{-1} at 77 K). Using a parallel triple exponential relaxation model, three non-equivalent SADS were extracted with ^{3}MLCT ESA features (Fig. 3 b) and e)), and the decay traces showing the fit at selected wavelengths are presented in c) and f)). The fastest decaying ESA component (k_1) covers the full spectral window, with the absorption feature spanning the bleach region. An equivalent process was not observed in the room-temperature data, likely due to overlap with competing ^{3}MLCT decay pathways. We speculate that it may arise from constrained ligand dynamics at low-temperature, or the appearance of a previously undetermined intermediate state, however, further investigation is required. Two further components with similar ESA features are revealed from data fitting, with decay rates of $\sim 10^6$ s^{-1} (k_2) and $\sim 10^5$ s^{-1} (k_3). The k_2 component includes both ESA and GSB relaxation, which is attributed to relaxation via ^{3}MLCT states within the manifold with greater singlet character.[40] The final decay component (k_3), spectrally distinct from k_2, is attributed to the remaining ^{3}MLCT manifold states undergoing non-radiative de-activation and phosphorescence.

Phosphorescence decay kinetics were also obtained at 77 K for both complexes. Reasonable fits of the data were obtained using three exponential components with rate constants of $\sim 4 \times 10^6$, $\sim 5 \times 10^5$, and $\sim 1 \times 10^5$ (Table S10). The ^{3}MC state is not expected to be thermally populated at 77 K, and the similarity in kinetics between the two complexes suggests that the ^{3}MLCT transitions are of the same nature for both compounds. k_2 obtained from the TA measurements is in general agreement with the fastest decay component of the emission data (accounting for the ∼10 ns response time of the time-resolved emission instrument), while k_3 from TA effectively tracks the average dynamics of the SOC states with μs lifetimes, with small differences arising from the detection modes (ESA vs emission). SOC-corrected triplet energies were calculated with several different functionals (BP86,[47] and PBE0[48]) in ORCA,[49] and the adjacent states were found to have splittings smaller than 50 cm^{-1}, making them impossible to resolve spectrally with our apparatus (SI Section 2.7). Another interesting feature is that the transient spectra of the mesocate showed

more distinct shoulder-like features at $\sim$ 530 nm. It is likely that the transient spectra of the two non-equivalent MLCT states (separated by 215 cm^{-1}) are overlapped due to geometric asymmetry.

Table 2: TA decay parameters based on a triple exponential analysis

parameters	k_1 (10^8 s^{-1})	k_2 (10^6 s^{-1})	k_3 (10^5 s^{-1})
Helicate	14.587 (0.001)[a]	6.77 (0.75)	1.57 (0.06)
Mesocate	5.247 (0.001)	2.43 (0.15)	1.22 (0.03)

[a] 2σ confidence bounds are given by covariance matrix

DFT calculations

The ground state singlet and triplet geometries (^{3}MLCT and ^{3}MC) for both complexes were optimized with PBE0/def2-SVP[48] with GD3 dispersion[50] in the Conductor-like Polarizable Continuum Model (CPCM) *n*-butyronitrile environment (no imaginary frequencies present) using the Gaussian16 program package.[51] The PBE0 functional has previously been shown to predict physical parameters of Ru(II) complexes with reasonable accuracy verified by comparison with X-ray crystallography structures.[52–54] Optimized ground state geometries are compared against the crystal structure in Table S1; the Ru-N bond lengths obtained from DFT structures are generally shorter than those in the crystal structure, but the deviations in bond lengths between calculated and crystal structures are mostly less than 1%. The Ru-Ru distance for the helicate is 1.65 Å shorter than the mesocate. CPCM of the compounds in acetonitrile and gas phase structures were also calculated; no significant differences in the structures and energies were observed by changing CPCM solvent from *n*-butyronitrile to acetonitrile, but the gas phase ^{3}MLCT states generally have shorter Ru-N bond lengths (Table S2). The lowest triplet states have a Ru-N distance slightly elongated by $\sim$ 0.04 Å, the opposite Ru-N bond is shortened very slightly by 0.015 Å which is similar to other Ru polypyridyl complexes reported previously optimized with double-hybrid functionals.[15,45,46] Both the bond length change and the Mulliken spin densities ($\sim$0.9) are located on a single ruthenium center, suggesting that the calculated triplet is localized, and of ^{3}MLCT charac-

ter.[41] This is further validated upon examining the natural transition orbitals of the adiabatic ^{3}MLCT→GS transition (SI Section 2.6). Vertical transition energies were calculated using the DFT (UPBE0) optimized ^{3}MLCT and GS geometries, electronic energies, and zero-point energy (ZPE) corrections. Similar to experimental results, the predicted emission energies of the two complexes are almost identical with similar bond displacements. However, the optimized ^{3}MC (*dd*) states were noticeably different between the isomers. The helicate ^{3}MC state adopted a structure with an axial Ru-N bond 0.121 Å longer than the ^{3}MLCT state, and it is energetically above the ^{3}MLCT state. Smaller bond elongation occurs on both axial Ru-N bonds for the mesocate, with the *dd* state lying below the ^{3}MLCT state. This axial distortion is expected to be stabilized by the Jahn-Teller effect since in the ^{3}MC state the e_g orbital is asymmetrically occupied.[55] An attempt was made to use the Ru-N bond lengths converged for the mesocate as the starting geometry for the helicate, and the structure converged back to the ^{3}MLCT state. The reverse was also done and led to convergence failure of the mesocate structure or the structure converged back to the ^{3}MLCT state. Fig. 4 shows TD-DFT (green) and self-consistent field (SCF) interpolated energies (purple curve) from the ^{3}MLCT state to the ^{3}MC state for the helicate in sub-figure b) and for the mesocate in d). The horizontal axis represents the change in the molecular geometry and is normalized. The ^{3}MLCT state is reached with smaller geometry distortion and further displacement leads to the ^{3}MC state with the ΔE_{TS} being an upper limit of the energy barrier for interconversion between the two states. ΔE_{T-T}, the energy difference between the ^{3}MC state and the ^{3}MLCT state, shows that the ^{3}MC state lies 850 cm^{-1} above the ^{3}MLCT state for the helicate. For the mesocate, the ^{3}MC state is 520 cm^{-1} below the ^{3}MLCT state. At the ^{3}MC geometry, the energy separation between the triplet energy curve and the ground state is significantly smaller for the mesocate compared to the helicate (the TD-DFT interpolated curve of the triplet state crosses with the interpolated curve of the singlet ground state - this normally suggests photo-dissociation, but negligible photo-dissociation has been observed experimentally (see SI section 3.4)).

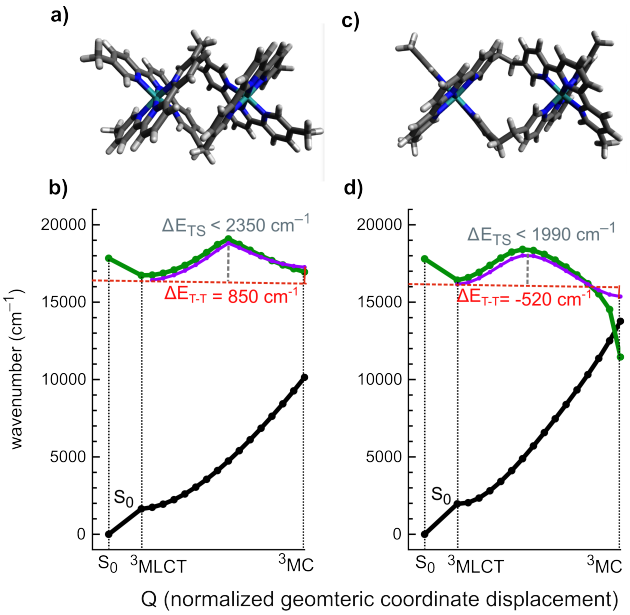

Figure 4: The structures of helicate a) and mesocate c) with the interpolated ground state and triplet state potential energy curves using TD-PBE0/def2SVP (green) and ground state SCF PBE0/def2SVP (purple) in b) and d) for the two complexes, respectively. The first point on each graph is based on the ground state SCF energy of the S_0 state and TD-PBE0/def2-SVP calculation to the first excited triplet state.

The nature of electronic transitions was further investigated by TD-DFT (TD-PBE0/def2-SVP) calculations. The MOs involved in the singlet-singlet transitions (^{1}MLCT $\leftarrow$ GS) with appreciable oscillator strengths are presented in the SI Section 2.5. The occupied orbitals are metal-based t_{2g} orbitals and the unoccupied orbitals are mostly of π^* character on the ligand with the orbitals at lower energies mixed with d orbitals. The mixing of π^* with d orbitals has been reported for polypyridylruthenium(II) complexes in Khon-Sham orbital calculations.[45] For the helicate, the orbitals involved are delocalized across both Ru centers but for the mesocate, the orbitals are mostly localized on one center.

The natural transition orbitals (NTOs) for the vertical excitation from the ground state to the optimized triplet states show that the ^{3}MLCT $\rightarrow$ GS transition is localized on a single Ru center. For the helicate, the energy separation of the triplet states located on the two centers is very small $\sim$ 30 cm^{-1}. For the mesocate, the separation is about 215 cm^{-1}, (SI

Section 2.6) and is likely due to the 0.003 Å difference in Ru-N bond lengths between the two centers (Table S1).

Conclusions

In summary, the photophysics of the helicate and the mesocate diastereoisomers of double-stranded polypyridylruthenium(II) complexes have been characterized at room temperature and cryogenic temperatures. We show the luminescence quenching at room temperature arises from an energetically proximal ^{3}MC state and a higher ^{3}MLCT state with greater singlet character. The mesocate was more distorted from the octahedral coordination environment near the bridge, resulting in the ^{3}MC state lying below the lowest ^{3}MLCT state, causing faster excited-state relaxation. Calculated relative energies between the triplet ^{3}MC and ^{3}MLCT states were in qualitative agreement with fitted rate constants. TAS and time-resolved emission experiments at 77 K also resolved ^{3}MLCT states related to each other by SOC, with one order of magnitude difference in the rate of decay. Some spectral features in transient measurements hinted at excited state delocalization or charge transfer, however, further investigation is required. This work could be useful for exploring different ligand engineering strategies for dinuclear metal complexes to subtly tune their photophysical properties to suit applications in biological imaging or targeted cancer detection or therapy.

Experimental details

General:

The complexes were prepared using previously reported methods.[31] Spectroscopy grade acetonitrile (Sigma Aldrich) was used for room-temperature transient absorption measurements. The solvent *n*-butyronitrile (Sigma Aldrich) was checked to ensure no impurities affected experimental results by performing TA and steady-state measurements on the solvent only at both room temperature and 77K. Solvent glass scattered light (time-independent) was

subtracted for cryogenic data analysis. All experiments except steady-state absorption were done with ∼200 μM de-aerated solutions in graded-seal 2mm path length cuvettes and the absorption at the excitation wavelength was ∼0.25. For cryogenic measurements, the samples were cooled with a liquid nitrogen cryostat (Optistat DN, Oxford Instruments) with the liquid nitrogen valve open to constantly cool the sample at 77K during measurements.

Steady-state spectroscopy:

Steady-state absorption spectra were recorded from ∼50 μM samples in aerated *n*-butyronitrile in 1 cm path-length quartz cuvettes using a UV-vis spectrometer (Cary 50 Bio) with (scan rate 300 nm/min, averaging time 0.10 s, bandwidth 1 nm).

Steady-state emission spectra and excitation-emission matrices were measured in synchronous scan mode for cryogenically cooled samples with a commercial fluorimeter (Cary Eclipse, PMT voltage 600 V, excitation and emission bandwidths 10 nm, scan rate 120 nm/min). The emission spectra were obtained by front-face measurements where the 2 mm path-length graded-seal quartz cuvette was placed at 45 degrees relative to the excitation beam.

Transient absorption measurements:

TA experiments were performed with a home-built pump-probe spectrometer based on a dual amplifier arrangement (details see SI Section 3.1). This ensured exactly the same excitation pulse conditions were used for all TA timescales. Room temperature measurements were performed at a pulse repetition rate of 50kHz with mechanical delay only (35 nJ/pulse; pump, probe spot sizes in FWHM: 480 and 175 μm). 77K measurements were carried out at 5kHz pulse repetition rate with both mechanical and electronic delays (40 nJ/pulse for the mesocate and 60 nJ/pulse for the helicate; pump, probe spot sizes in FWHM: 490 and 190 μm).

Emission decay measurements:

The experimental setup used for time-resolved emission measurements is described elsewhere.[56] The excitation power was 15.5 mW at 10 Hz at 477 nm (spot size ∼ 0.4 cm FWHM,

1.5 mJ/pulse).

Acknowledgement

This work was supported by the Australian Government through the Australian Research Council (ARC) under the Centre of Excellence (CE170100026) and Linkage and Equipment (LE200100051) schemes. C.H. is the recipient of an Australian Research Council Future Fellowship (FT210100113), funded by the Australian Government.

We also acknowledge support through the University of Melbourne Spartan High-Performance Computing facility.

Supporting Information Available

Supplementary information available for detailed experimental methods and computational results.

References

(1) Young, R. C.; Meyer, T. J.; Whitten, D. G. Kinetic relaxation measurement of rapid electron transfer reactions by flash photolysis. Conversion of light energy into chemical energy using the tris(2,2′-bipyridine)ruthenium(3+)-tris(2,2′-bipyridine)ruthenium(2+*) couple. *Journal of the American Chemical Society* **1975**, *97*, 4781–4782.

(2) Juris, A.; Balzani, V.; Barigelletti, F.; Campagna, S.; Belser, P.; von Zelewsky, A. Ru(II) polypyridine complexes: photophysics, photochemistry, eletrochemistry, and chemiluminescence. *Coordination Chemistry Reviews* **1988**, *84*, 85–277.

(3) Morris, A. J.; Meyer, G. J.; Fujita, E. Molecular Approaches to the Photocatalytic

Reduction of Carbon Dioxide for Solar Fuels. *Accounts of Chemical Research* **2009**, *42*, 1983–1994, PMID: 19928829.

(4) Meyer, T. J. Chemical approaches to artificial photosynthesis. *Accounts of Chemical Research* **1989**, *22*, 163–170.

(5) Prajith, N.; Priyanka, P.; Alexander, V. Synthesis, characterization, photophysical, lipophilicity, and in vitro fluorescence studies of mono-, di-, and trinuclear Ru (II) polypyridyl complexes of pyridinyl benzimidazole derivatives. *JBIC Journal of Biological Inorganic Chemistry* **2022**, *27*, 357–372.

(6) Pashaei, B.; Shahroosvand, H.; Moharramnezhad, M.; Kamyabi, M. A.; Bakhshi, H.; Pilkington, M.; Nazeeruddin, M. K. Two in One: A Dinuclear Ru(II) Complex for Deep-Red Light-Emitting Electrochemical Cells and as an Electrochemiluminescence Probe for Organophosphorus Pesticides. *Inorganic Chemistry* **2021**, *60*, 17040–17050.

(7) Sakurai, H.; Jacquet, M.; Lafolet, F.; Loiseau, F.; Saint-Aman, E.; Royal, G.; Cobo, S. Photochemical and photophysical properties of photochromic osmium terpyridine-dimethyldihydropyrene complexes. *Dyes and Pigments* **2019**, *160*, 93–98.

(8) Zhao, H.; Xu, X.; Wang, S.; Mi, Y.; Zheng, Z.; Zhao, X. A dinuclear ruthenium (II) complex as an inducer and potential luminescent switch-on probe for G-quadruplex DNA. *Transition Metal Chemistry* **2018**, *43*, 539–548.

(9) Ning, Y.; Jin, G. Q.; Wang, M. X.; Gao, S.; Zhang, J. L. Recent progress in metal-based molecular probes for optical bioimaging and biosensing. *Current Opinion in Chemical Biology* **2022**, *66*, 102097–102097.

(10) Gill, M. R.; Thomas, J. A. Ruthenium(II) polypyridyl complexes and DNA-from structural probes to cellular imaging and therapeuticsw. *Chem. Soc. Rev* **2012**, *41*, 3179–3192.

(11) Constable, E. C.; Thompson, A. M. C.; Armaroli, N.; Balzani, V.; Maestri, M. Ligand substitution patterns control photophysical properties of ruthenium (II)-2, 2′: 6′, 2″-terpyridine complexes—room temperature emission from $[Ru(tpy)_2]^{2+}$ analogues. *Polyhedron* **1992**, *11*, 2707–2709.

(12) Amini, A.; Harriman, A.; Mayeux, A. The triplet excited state of ruthenium(ii) bis(2,2′:6′,2″-terpyridine): Comparison between experiment and theory. *Physical Chemistry Chemical Physics* **2004**, 1157–1164.

(13) Rupp, M. T.; Shevchenko, N.; Hanan, G. S.; Kurth, D. G. Enhancing the photophysical properties of Ru(II) complexes by specific design of tridentate ligands. *Coordination Chemistry Reviews* **2021**, *446*, 214127–214127.

(14) Thompson, D. W.; Ito, A.; Meyer, T. J. $[Ru(bpy)_3]^{2+*}$ and other remarkable metal-to-ligand charge transfer (MLCT) excited states. *Pure and Applied Chemistry* **2013**, *85*, 1257–1305.

(15) Alcover-Fortuny, G.; Wu, J.; Caballol, R.; De Graaf, C. Quantum Chemical Study of the Interligand Electron Transfer in Ru Polypyridyl Complexes. *Journal of Physical Chemistry A* **2018**, *122*.

(16) Vallett, P. J.; Damrauer, N. H. Experimental and computational exploration of ground and excited state properties of highly strained ruthenium terpyridine complexes. *Journal of Physical Chemistry A* **2013**, *117*, 6489–6507.

(17) Sun, Q.; Dereka, B.; Vauthey, E.; Lawson Daku, L. M.; Hauser, A. Ultrafast transient IR spectroscopy and DFT calculations of ruthenium(II) polypyridyl complexes. *Chemical Science* **2017**, *8*, 223–230.

(18) Hewitt, J. T.; Vallett, P. J.; Damrauer, N. H. Dynamics of the ^{3}MLCT in Ru(II) terpyridyl complexes probed by ultrafast spectroscopy: Evidence of excited-state equi-

libration and interligand electron transfer. *Journal of Physical Chemistry A* **2012**, *116*, 11536–11547.

(19) Sun, Q.; Mosquera-Vazquez, S.; Lawson Daku, L. M.; Guénée, L.; Goodwin, H. A.; Vauthey, E.; Hauser, A. Experimental evidence of ultrafast quenching of the ^{3}MLCT luminescence in ruthenium(II) tris-bipyridyl complexes via a ^{3}dd state. *Journal of the American Chemical Society* **2013**, *135*, 13660–13663.

(20) Harriman, A.; Mayeux, A.; Stroh, C.; Ziessel, R. Photophysical properties of binuclear ruthenium(II) bis(2,2′: 6′,2″-terpyridine) complexes built around a central 2,2′-bipyrimidine receptor. *Dalton Transactions* **2005**, 2925–2932.

(21) Zhang, Y.; Uahengo, V.; Cai, P.; Cheng, Z. Chemistry Synthesis, characterization, and antitumor activity of mononuclear and dinuclear ruthenium complexes Synthesis, characterization, and antitumor activity of mononuclear and dinuclear ruthenium complexes. *Journal of Coordination Chemistry* **2018**, *71*, 2091–2101.

(22) Tan, S. S.; Yanagisawa, S.; Inagaki, K.; Kassim, M. B.; Morikawa, Y. Experimental and computational studies on ruthenium(ii) bis-diimine complexes of N, N ′-chelate ligands: The origin of changes in absorption spectra upon oxidation and reduction. *Physical Chemistry Chemical Physics* **2019**, *21*, 7973–7988.

(23) Kreitner, C.; Grabolle, M.; Resch-Genger, U.; Heinze, K. Dual emission and excited-state mixed-valence in a quasi-symmetric dinuclear Ru-Ru complex. *Inorganic Chemistry* **2014**, *53*, 12947–12961.

(24) Wang, F.; Yang, L.; Xian, X.-Q. Comparison Between Binuclear and Mononuclear Ru (II) Complexes: Synthesis, Structure, Photophysics, and Oxygen Sensing Performance. *Frontiers in chemistry* **2021**, *9*.

(25) De Cola, L.; Belser, P. Photoinduced energy and electron transfer processes in rigidly

bridged dinuclear Ru/Os complexes. *Coordination Chemistry Reviews* **1998**, *177*, 301–346.

(26) Wouters, K. L.; De Tacconi, N. R.; Konduri, R.; Lezna, R. O.; MacDonnell, F. M. Driving multi-electron reactions with photons: Dinuclear ruthenium complexes capable of stepwise and concerted multi-electron reduction. *Photosynthesis Research* **2006**, *87*, 41–55.

(27) Li, G.; Zhu, D.; Wang, X.; Su, Z.; Bryce, M. R. Dinuclear metal complexes: multifunctional properties and applications. *Chem. Soc. Rev* **2020**, *49*, 765–765.

(28) Li, R.; Dalton, .; Gamache, M. T.; Auvray, T.; Kurth, D. G.; Hanan, G. S. Dinuclear 2,4-di(pyridin-2-yl)-pyrimidine based ruthenium photosensitizers for hydrogen photoevolution under red light. *Dalton Trans* **2021**, *50*, 16528–16528.

(29) Ward, M. D. 18 Supramolecular coordination chemistry. *Annu. Rep. Prog. Chem., Sect. A: Inorg. Chem.* **2000**, *96*, 345–385.

(30) Shankar, B.; Sahu, S.; Deibel, N.; Schweinfurth, D.; Sarkar, B.; Elumalai, P.; Gupta, D.; Hussain, F.; Krishnamoorthy, G.; Sathiyendiran, M. Luminescent dirhenium(I)-double-heterostranded helicate and mesocate. *Inorganic Chemistry* **2014**, *53*, 922–930.

(31) Flint, K. L.; Collins, J. G.; Bradley, S. J.; Smith, T. A.; Sumby, C. J.; Keene, F. R. Synthesis and Characterisation of Helicate and Mesocate Forms of a Double-Stranded Diruthenium(II) Complex of a Di(terpyridine) Ligand. *Australian Journal of Chemistry* **2019**, *72*, 762–768.

(32) Allison, S. J.; Cooke, D.; Davidson, F. S.; Elliott, P. I. P.; Faulkner, R. A.; Griffiths, H. B. S.; Harper, O. J.; Hussain, O.; Owen-Lynch, P. J.; Phillips, R. M. et al. Ruthenium-Containing Linear Helicates and Mesocates with Tuneable p53-Selective Cytotoxicity in Colorectal Cancer Cells. *Angewandte Chemie - International Edition* **2018**, *57*, 9799–9804.

(33) Thompson, D. W.; Wishart, J. F.; Brunschwig, B. S.; Sutin, N. Efficient generation of the ligand field excited state of tris-(2,2′-bipyridine)-ruthenium(II) through sequential two-photon capture by $[Ru(bpy)_3]^{2+}$ or electron capture by $[Ru(bpy)_3]^{3+}$. *Journal of Physical Chemistry A* **2001**, *105*, 8117–8122.

(34) Liu, Y.; Hammitt, R.; Lutterman, D. A.; Thummel, R. P.; Turro, C. Marked differences in light-switch behavior of Ru(II) complexes possessing a tridentate DNA intercalating ligand. *Inorganic Chemistry* **2007**, *46*, 6011–6021.

(35) Abrahamsson, M.; Becker, H.-C.; Hammarström, L.; Bonnefous, C.; Chamchoumis, C.; Thummel, R. P. Six-Membered Ring Chelate Complexes of Ru(II): Structural and Photophysical Effects. *Inorganic Chemistry* **2007**, *46*, 10354–10364.

(36) Alemán, E. A.; Shreiner, C. D.; Rajesh, C. S.; Smith, T.; Garrison, S. A.; Modarelli, D. A. Photoinduced electron-transfer within osmium(II) and ruthenium(II) bis-terpyridine donor acceptor dyads. *Dalton Transactions* **2009**, 6562–6577.

(37) Hammarström, L.; Barigelletti, F.; Flamigni, L.; Indelli, M. T.; Armaroli, N.; Calogero, G.; Guardigli, M.; Sour, A.; Collin, J.-P.; Sauvage, J.-P. A study on delocalization of MLCT excited states by rigid bridging ligands in homometallic dinuclear complexes of ruthenium (II). *The Journal of Physical Chemistry A* **1997**, *101*, 9061–9069.

(38) Karmakar, S.; Maity, D.; Mardanya, S.; Baitalik, S. Multichromophoric bimetallic Ru(II) terpyridine complexes based on pyrenyl-bis-phenylimidazole spacer: Synthesis, photophysics, spectroelectrochemistry, and TD-DFT calculations. *Inorganic Chemistry* **2014**, *53*, 12036–12049.

(39) Lumpkin, R. S.; Kober, E. M.; Worl, L. A.; Murtaza, Z.; Meyer, T. J. Metal-to-ligand charge-transfer (MLCT) photochemistry: experimental evidence for the participation

of a higher lying MLCT state in polypyridyl complexes of ruthenium (II) and osmium (II). *Journal of Physical Chemistry* **1990**, *94*, 239–243.

(40) Henchman, D. M. J.; Lumpkin, R. S.; Kober, E. M.; Worl, L. A.; Murtaza, Z.; Meyer, T. J. Experimental Evidence for the Participation of a Higher Lying MLCT State in Polypyridyl Complexes of Ruthenium(II) and Osmium(II). *J. Phys. Chem* **1990**, *94*, 76092–76134.

(41) Sun, Q.; Mosquera-Vazquez, S.; Suffren, Y.; Hankache, J.; Amstutz, N.; Lawson Daku, L. M.; Vauthey, E.; Hauser, A. On the role of ligand-field states for the photophysical properties of ruthenium(II) polypyridyl complexes. *Coordination Chemistry Reviews* **2015**, *282-283*, 87–99.

(42) Benniston, A. C.; Harriman, A.; Li, P.; Patel, P. V.; Rostron, J. P.; Sams, C. A. An apparent angle dependence for the nonradiative deactivation of excited triplet states of sterically constrained, binuclear ruthenium(II) bis(2,2′:6′,2″-terpyridine) complexes. *Journal of Physical Chemistry A* **2006**, *110*, 9880–9886.

(43) Barigelletti, F.; Belser, P.; Von Zelewsky, A.; Juris, A.; Balzani, V. Luminescence of mixed-ligand polypyridine-ruthenium (II) complexes in the temperature range 84-250 K. Interligand interactions and viscosity effects on radiationless processes. *The Journal of Physical Chemistry* **1985**, *89*, 3680–3684.

(44) Thompson, D. W.; Fleming, C. N.; Myron, B. D.; Meyer, T. J. Rigid Medium Stabilization of Metal-to-Ligand Charge Transfer Excited States. *The Journal of Physical Chemistry B* **2007**, *111*, 6930–6941.

(45) Borg, O. A.; Godinho, S. S. M. C.; Lundqvist, M. J.; Lunell, S.; Persson, P. Computational Study of the Lowest Triplet State of Ruthenium Polypyridyl Complexes Used in Artificial Photosynthesis. *The Journal of Physical Chemistry A* **2008**, *112*, 4470–4476, PMID: 18426189.

(46) Jakubikova, E.; Chen, W.; Dattelbaum, D. M.; Rein, F. N.; Rocha, R. C.; Martin, R. L.; Batista, E. R. Electronic structure and spectroscopy of $[Ru(tpy)_2]^{2+}$, $[Ru(tpy)(bpy)(H_2O)]^{2+}$, and $[Ru(tpy)(bpy)(Cl)]^{+}$. *Inorganic Chemistry* **2009**, *48*, 10720–10725.

(47) Becke, A. D. Density-functional exchange-energy approximation with correct asymptotic behavior. *Physical review A* **1988**, *38*, 3098.

(48) Perdew, J. P.; Ernzerhof, M.; Burke, K. Rationale for mixing exact exchange with density functional approximations. *The Journal of Chemical Physics* **1996**, *105*, 9982–9985.

(49) Hočevar, T.; Demšar, J. Computation of Graphlet Orbits for Nodes and Edges in Sparse Graphs. *Journal of Statistical Software* **2016**, *71*, 1–24.

(50) Grimme, S.; Antony, J.; Ehrlich, S.; Krieg, H. A consistent and accurate ab initio parametrization of density functional dispersion correction (DFT-D) for the 94 elements H-Pu. *The Journal of Chemical Physics* **2010**, *132*, 154104.

(51) Frisch, M. J.; Trucks, G. W.; Schlegel, H. B.; Scuseria, G. E.; Robb, M. A.; Cheeseman, J. R.; Scalmani, G.; Barone, V.; Petersson, G. A.; Nakatsuji, H. et al. Gaussian 16 Revision C.01. 2016; Gaussian Inc. Wallingford CT 2009.

(52) Österman, T.; Abrahamsson, M.; Becker, H. C.; Hammarström, L.; Persson, P. Influence of triplet state multidimensionality on excited state lifetimes of bis-tridentate Ru(II) complexes: A computational study. *Journal of Physical Chemistry A* **2012**, *116*, 1041–1050.

(53) Fahim, Z. M. E.; Bouzzine, S. M.; Youssef, A. A.; Bouachrine, M.; Hamidi, M. Ground state geometries, UV/vis absorption spectra and charge transfer properties of triphenylamine-thiophenes based dyes for DSSCs: A TD-DFT benchmark study. *Computational and Theoretical Chemistry* **2018**, *1125*, 39–48.

(54) Maschietto, F.; Campetella, M.; Sanz García, J.; Adamo, C.; Ciofini, I. Chasing unphysical TD-DFT excited states in transition metal complexes with a simple diagnostic tool. *Journal of Chemical Physics* **2021**, *154*.

(55) Conradie, J. Jahn-Teller effect in high spin d^4 and d^9 octahedral metal-complexes. *Inorganica Chimica Acta* **2019**, *486*, 193–199.

(56) Nathanael, J. G.; Yuan, B.; Hall, C. R.; Smith, T. A.; Wille, U. Damage of amino acids by aliphatic peroxyl radicals: a kinetic and computational study. *Org. Biomol. Chem.* **2023**, *21*, 2390–2397.